EXTENDED PDF FORMAT
SPONSORED BY
SIGMA®
Life Science
sigma.com/knockout

Science
AAAS

Revealing the Superfluid Lambda Transition in the Universal Thermodynamics of a Unitary Fermi Gas

Mark J. H. Ku, *et al.*

Science **335**, 563 (2012);
DOI: 10.1126/science.1214987

This copy is for your personal, non-commercial use only.

If you wish to distribute this article to others, you can order high-quality copies for your colleagues, clients, or customers by clicking here.

Permission to republish or repurpose articles or portions of articles can be obtained by following the guidelines here.

The following resources related to this article are available online at www.sciencemag.org (this infomation is current as of February 20, 2012):

Updated information and services, including high-resolution figures, can be found in the online version of this article at:
http://www.sciencemag.org/content/335/6068/563.full.html

Supporting Online Material can be found at:
http://www.sciencemag.org/content/suppl/2012/01/12/science.1214987.DC1.html

A list of selected additional articles on the Science Web sites **related to this article** can be found at:
http://www.sciencemag.org/content/335/6068/563.full.html#related

This article **cites 37 articles**, 2 of which can be accessed free:
http://www.sciencemag.org/content/335/6068/563.full.html#ref-list-1

This article has been **cited by** 1 articles hosted by HighWire Press; see:
http://www.sciencemag.org/content/335/6068/563.full.html#related-urls

This article appears in the following **subject collections:**
Physics
http://www.sciencemag.org/cgi/collection/physics

Downloaded from www.sciencemag.org on February 20, 2012

Science (print ISSN 0036-8075; online ISSN 1095-9203) is published weekly, except the last week in December, by the American Association for the Advancement of Science, 1200 New York Avenue NW, Washington, DC 20005. Copyright 2012 by the American Association for the Advancement of Science; all rights reserved. The title *Science* is a registered trademark of AAAS.

will slow down their spin rates with time after the RLDP. However, they cannot explain the apparent difference in spin distributions between AXMSPs and radio MSPs, because radio MSPs, which have weak surface magnetic field strengths, could not spin down by the required amount even in a Hubble time. The true age of a pulsar (*23*) is given by $t = P/((n-1)\dot{P})[1-(P_0/P)^{n-1}]$. Assuming an evolution with a braking index $n = 3$ and $B = 1.0\times 10^8$ G, the time scale t is larger than 10 Gy, using $P_0 = \langle P\rangle_{\rm AXMSP} = 3.3$ ms and $P(t) = \langle P\rangle_{\rm MSP} = 5.5$ ms. To make things worse, one has to add the main-sequence lifetime of the LMXB donor star, which is typically 3 to 12 Gy, thereby reaching unrealistic large total ages. Although the statistics of AXMSPs still has its basis in small numbers and care must be taken for both detection biases (such as eclipsing effects of radio MSPs) and comparison between various subpopulations (*8*), it is evident from both observations and theoretical work that the RLDP effect presented here plays an important role for the spin distribution of MSPs.

The RLDP effect may also help explain a few other puzzles, for example, why characteristic (or spin-down) ages of radio MSPs often largely exceed cooling age determinations of their white dwarf companions (*24*). It has been suggested that standard cooling models of white dwarfs may not be correct (*25*–*27*), particularly for low-mass helium white dwarfs. These white dwarfs avoid hydrogen shell flashes at early stages and retain thick hydrogen envelopes, at the bottom of which residual hydrogen burning can continue for several billion years after their formation, keeping the white dwarfs relatively hot (~10^4 K) and thereby appearing much younger than they actually are. However, it is well known that the characteristic age is not a trustworthy measure of true age (*28*), and the RLDP effect exacerbates this discrepancy even further. In the model calculation presented in Fig. 1, it was assumed that $B = 1.0\times 10^8$ G and $\varphi = 1.0$. However, P_0 and τ_0 depend strongly on both B and φ. This is shown in Fig. 2, where I have calculated the RLDP effect for different choices of B and φ by using the same stellar donor model [i.e., same $\dot{M}(t)$ profile] as before. The use of other LMXB donor star masses, metallicities, and initial orbital periods would lead to other $\dot{M}(t)$ profiles (*16*, *17*) and hence different evolutionary tracks. The conclusion is that recycled MSPs can basically be born with any characteristic age. Thus, we are left with the cooling age of the white dwarf companion as the sole reliable, although still not accurate, measure as an age indicator.

A final puzzle is why no sub-millisecond pulsars have been found among the 216 radio MSPs detected in total so far. Although modern observational techniques are sensitive enough to pick up sub-millisecond radio pulsations, the fastest spinning known radio MSP, J1748−2446ad (*29*), has a spin frequency of only 716 Hz, corresponding to a spin period of 1.4 ms. This spin rate is far from the expected minimum equilibrium spin period (*8*) and the physical mass shedding limit of about 1500 Hz. It has been suggested that gravitational wave radiation during the accretion phase halts the spin period above a certain level (*30*, *31*). The RLDP effect presented here is a promising candidate for an alternative mechanism, in case a sub-millisecond AXMSP is detected (*8*).

References and Notes

1. M. A. Alpar, A. F. Cheng, M. A. Ruderman, J. Shaham, *Nature* **300**, 728 (1982).
2. D. Bhattacharya, E. P. J. van den Heuvel, *Phys. Rep.* **203**, 1 (1991).
3. L. Bildsten *et al.*, *Astrophys. J. Suppl. Ser.* **113**, 367 (1997).
4. R. Wijnands, M. van der Klis, *Nature* **394**, 344 (1998).
5. J. W. T. Hessels *et al.*, *AIP Conf. Proc.* **1068**, 130 (2008).
6. The Roche lobe of a binary star is the innermost equipotential surface passing through the first Lagrangian point, L1. If a star fills its Roche lobe, the unbalanced pressure at L1 will cause mass transfer to the other star (*2*).
7. A. M. Archibald *et al.*, *Science* **324**, 1411 (2009); 10.1126/science.1172740.
8. Materials and methods are available as supporting material on *Science* Online.
9. F. K. Lamb, C. J. Pethick, D. A. Pines, *Astrophys. J.* **184**, 271 (1973).
10. P. Ghosh, F. K. Lamb, *NATO Sci. Ser.* **377**, 487 (1992).
11. J. Frank, A. King, D. J. Raine, *Accretion Power in Astrophysics* (Cambridge Univ. Press, Cambridge, 2002).
12. A. F. Illarionov, R. A. Sunyaev, *Astron. Astrophys.* **39**, 185 (1975).
13. M. Ruderman, J. Shaham, M. Tavani, *Astrophys. J.* **336**, 507 (1989).
14. R. F. Webbink, S. Rappaport, G. J. Savonije, *Astrophys. J.* **270**, 678 (1983).
15. S. Rappaport, Ph. Podsiadlowski, P. C. Joss, R. Di Stefano, Z. Han, *Mon. Not. R. Astron. Soc.* **273**, 731 (1995).
16. T. M. Tauris, G. J. Savonije, *Astron. Astrophys.* **350**, 928 (1999).
17. Ph. Podsiadlowski, S. Rappaport, E. D. Pfahl, *Astrophys. J.* **565**, 1107 (2002).
18. The magnetospheric coupling parameter, $0.5 < \varphi < 1.4$ is a numerical factor of order unity depending on the accretion flow, the disk model, and the magnetic inclination angle of the pulsar (*10*, *11*, *32*–*34*).
19. S. L. Shapiro, S. A. Teukolsky, *Black Holes, White Dwarfs, and Neutron Stars: The Physics of Compact Objects* (Wiley-Interscience, New York, 1983).
20. S. A. Rappaport, J. M. Fregeau, H. C. Spruit, *Astrophys. J.* **606**, 436 (2004).
21. L. Burderi *et al.*, *Astrophys. J.* **560**, L71 (2001).
22. This "turn-off problem" has previously been debated elsewhere (*13*, *33*, *35*).
23. R. N. Manchester, J. H. Taylor, *Pulsars* (Freeman, San Francisco, CA, 1977).
24. D. R. Lorimer, A. G. Lyne, L. Festin, L. Nicastro, *Nature* **376**, 393 (1995).
25. F. Alberts, G. J. Savonije, E. P. J. van den Heuvel, O. R. Pols, *Nature* **380**, 676 (1996).
26. L. A. Nelson, E. Dubeau, K. A. MacCannell, *Astrophys. J.* **616**, 1124 (2004).
27. M. H. van Kerkwijk, C. G. Bassa, B. A. Jacoby, P. G. Jonker, in *Binary Radio Pulsars*, F. A. Rasio, I. H. Stairs, Eds. [Astronomical Society of the Pacific (ASP) Conference Series, San Francisco, CA, 2005], vol. 328, pp. 357–370.
28. This is the case if the pulsar spin period, P, is close to its initial spin period, P_0.
29. J. W. T. Hessels *et al.*, *Science* **311**, 1901 (2006).
30. L. Bildsten, *Astrophys. J.* **501**, L89 (1998).
31. D. Chakrabarty *et al.*, *Nature* **424**, 42 (2003).
32. Y.-M. Wang, *Astrophys. J.* **475**, L135 (1997).
33. F. Lamb, W. Yu, in *Binary Radio Pulsars*, F. A. Rasio, I. H. Stairs, Eds. (ASP Conference Series, San Francisco, CA, 2005), vol. 328, pp. 299–310.
34. C. R. D'Angelo, H. C. Spruit, *Mon. Not. R. Astron. Soc.* **406**, 1208 (2010).
35. M. Ruderman, J. Shaham, M. Tavani, D. Eichler, *Astrophys. J.* **343**, 292 (1989).
36. A. Patruno, *Astrophys. J.* **722**, 909 (2010).
37. I. S. Shklovskii, *Sov. Astron.* **13**, 562 (1970).

Acknowledgments: I gratefully thank N. Langer and M. Kramer for discussions and funding and without whom these results would not be possible and R. Eatough for helpful comments on the SOM. This work was partly supported by the Cluster of Excellence proposal EXC 1076, "The nature of forces and matter," at the University of Bonn. Radio pulsar data has been obtained from the *ATNF Pulsar Catalogue* (www.atnf.csiro.au/research/pulsar/psrcat/).

Supporting Online Material

www.sciencemag.org/cgi/content/full/335/6068/561/DC1
Materials and Methods
SOM Text
Figs. S1 and S2
References (*38*–*54*)

8 November 2011; accepted 6 January 2012
10.1126/science.1216355

Revealing the Superfluid Lambda Transition in the Universal Thermodynamics of a Unitary Fermi Gas

Mark J. H. Ku, Ariel T. Sommer, Lawrence W. Cheuk, Martin W. Zwierlein*

Fermi gases, collections of fermions such as neutrons and electrons, are found throughout nature, from solids to neutron stars. Interacting Fermi gases can form a superfluid or, for charged fermions, a superconductor. We have observed the superfluid phase transition in a strongly interacting Fermi gas by high-precision measurements of the local compressibility, density, and pressure. Our data completely determine the universal thermodynamics of these gases without any fit or external thermometer. The onset of superfluidity is observed in the compressibility, the chemical potential, the entropy, and the heat capacity, which displays a characteristic lambda-like feature at the critical temperature $T_c/T_F = 0.167(13)$. The ground-state energy is $\frac{3}{5}\xi N E_F$ with $\xi = 0.376(4)$. Our measurements provide a benchmark for many-body theories of strongly interacting fermions.

Phase transitions are ubiquitous in nature: Water freezes into ice, electron spins suddenly align as materials turn into magnets, and metals become superconducting. Near the transitions, many systems exhibit critical behavior, reflected by singularities in thermodynamic quantities: The magnetic susceptibility diverges at a ferromagnetic transition, and the specific heat shows a jump at superconducting and superfluid transitions (*1*, *2*), resolved as the famous lambda peak in ^{4}He (*3*). A novel form of superfluidity has been realized in trapped, ultracold atomic gases of strongly interacting fermions, particles with half-integer spin (*4*–*7*). Thanks to an exquisite control over relevant system parameters, these gases have recently emerged as a versatile system well suited to solve open problems in many-body physics (*7*).

Initial measurements on the thermodynamics of strongly interacting Fermi gases have focused on trap-averaged quantities (*8*–*10*) in which the superfluid transition is inherently difficult to observe. The emergence of the condensate of fermion pairs in a spin-balanced Fermi gas is accompanied by only minute changes in the gas density (*5*). Quantities that involve integration of the density over the local potential, such as the energy E (*11*) and the pressure P (*12*), are only weakly sensitive to the sudden variations in the thermodynamics of the gas expected near the superfluid phase transition (*13*).

For a neutral gas, thermodynamic quantities involving the second derivative of the pressure P are expected to become singular at the second-order phase transition into the superfluid state. An example is the isothermal compressibility $\kappa = \frac{1}{n}\frac{\partial n}{\partial P}\big|_T$, the relative change of the gas density n due to a change in the pressure P. Because the change in pressure is related to the change in chemical potential μ of the gas via $\mathrm{d}P = n\,\mathrm{d}\mu$ at constant temperature, $\kappa = \frac{1}{n^2}\frac{\partial^2 P}{\partial \mu^2}\big|_T$ is a second derivative of the pressure, and thus should reveal a clear signature of the transition.

The general strategy to determine the thermodynamic properties of a given substance is to measure an equation of state (EoS), such as the pressure $P(\mu,T)$ as a function of the chemical potential μ and the temperature T. Equivalently, replacing the pressure by the density $n = \frac{\partial P}{\partial \mu}\big|_T$, one can determine the density EoS $n(\mu,T)$. We directly measure the local gas density $n(V)$ as a function of the local potential V from in situ absorption images of a trapped, strongly interacting Fermi gas of ^{6}Li atoms at a Feshbach resonance (*5*). The trapping potential is cylindrically symmetric, with harmonic confinement along the axial direction; this symmetry allows us to find the three-dimensional (3D) density through the inverse Abel transform of the measured column density (*14*, *15*). The local potential is directly determined from the atomic density distribution and the accurately known harmonic potential along the axial direction.

The compressibility κ follows as the change of the density n with respect to the local potential V experienced by the trapped gas. The change in the local chemical potential is given by the negative change in the local potential, $\mathrm{d}\mu = -\mathrm{d}V$, and hence the local compressibility is $\kappa = -\frac{1}{n^2}\frac{dn}{dV}\big|_T$. We can then replace the unknown chemical potential μ in the density EoS $n(\mu,T)$ by the known variation of n with μ in the atom trap, given by κ. Instead of the a priori unknown temperature T, we determine the pressure $P(V) = \int_{-\infty}^{\mu} \mathrm{d}\mu' n(\mu') = \int_V^{\infty} \mathrm{d}V' n(V')$ given by the integral of the density over the potential (*16*). The resulting equation of state $n(\kappa,P)$ contains only quantities that can be directly obtained from the density distribution. This represents a crucial advance over previous methods that require the input of additional thermodynamic quantities, such as the temperature T and the chemical potential μ, whose determination requires the use of a fitting procedure or an external thermometer, as in (*11*, *12*).

We normalize the compressibility and the pressure by the respective quantities at the same local density for a noninteracting Fermi gas at $T = 0$, $\kappa_0 = \frac{3}{2}\frac{1}{nE_F}$, and $P_0 = \frac{2}{5}nE_F$, where $E_F = \frac{\hbar^2(3\pi^2 n)^{2/3}}{2m}$ is the local Fermi energy and m is the particle mass, yielding $\tilde{\kappa} \equiv \kappa/\kappa_0$ and $\tilde{p} \equiv P/P_0$. For dilute gases at the Feshbach resonance, the scattering length diverges and is no longer a relevant length scale. In the absence of an interaction-dependent length scale, the thermodynamics of such resonant gases are universal (*17*), and $\tilde{\kappa}$ is a universal function of $\tilde{p}$ only. Every experimental profile $n(V)$, irrespective of the trapping potential, the total number of atoms, or the temperature, must produce the same universal curve $\tilde{\kappa}$ versus $\tilde{p}$. By averaging many profiles, one obtains a low-noise determination of $\tilde{\kappa}(\tilde{p})$.

Our method has been tested on the noninteracting Fermi gas that can be studied in two independent ways: in spin-balanced gases near the zero-crossing of the scattering length and in the wings of highly imbalanced clouds at unitarity, where only one spin state is present locally. Both determinations yield the same noninteracting compressibility EoS (Fig. 1).

Figure 1 also shows the compressibility equation of state $\tilde{\kappa}(\tilde{p})$ for the unitary Fermi gas. In the high-temperature ($\tilde{p} >> 1$) regime, the pressure, and hence all other thermodynamic quantities, allow for a Virial expansion in terms of the fugacity $e^{\beta\mu}$ (*18*): $P\,\beta\lambda^3 = 2\sum_j b_j\, e^{j\beta\mu}$, with the nth-order Virial coefficients b_n. It is known that $b_1 = 1$, $b_2 = 3\sqrt{2}/8$, and $b_3 = -0.29095295$ (*18*); our data show good agreement with the third-order Virial expansion. Fixing b_2 and b_3, our measurement yields a prediction for $b_4 = +0.065(10)$, in agreement with (*12*), but contradicting a recent four-body calculation that gives a negative sign (*19*).

At degenerate temperatures ($\tilde{p} \lesssim 1$), the normalized compressibility rises beyond that of a noninteracting Fermi gas, as expected for an attractively interacting gas. A sudden rise of the compressibility at around $\tilde{p} = 0.55$, followed by a decrease at lower temperatures marks the superfluid transition. The expected singularity of the compressibility at the transition is rounded off by the finite resolution of our imaging system. Below the transition point, the decrease of the compressibility is consistent with the expectation from Bardeen-Cooper-Schrieffer (BCS) theory, in which

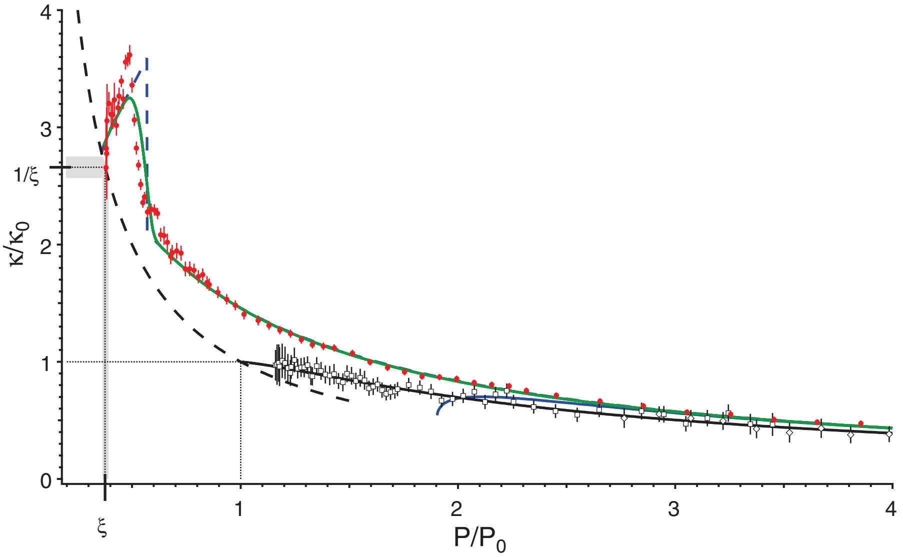

Fig. 1. Normalized compressibility κ/κ_0 versus normalized pressure P/P_0 of the unitary Fermi gas (red solid circles). Each data point is the average of between 30 and 150 profiles. The error bars show mean ± SD, including systematic errors from image calibration (*13*). Blue solid line: third-order Virial expansion. Black open squares (black open diamonds): data for a noninteracting Fermi gas obtained with a highly spin-imbalanced mixture at the Feshbach resonance (spin-balanced gas near zero-crossing of the scattering length). Black solid curve: theory for a noninteracting Fermi gas. Black dashed curve: the relation $\tilde{\kappa} = 1/\tilde{p}$ that must be obeyed at zero temperature both for the noninteracting gas ($\tilde{\kappa} = 1/\tilde{p} = 1$) and the unitary gas ($\tilde{\kappa} = 1/\tilde{p} = 1/\xi$) (dotted lines). Gray band: the uncertainty region for the $T = 0$ value of $\tilde{\kappa} = 1/\xi$ and $\tilde{p} = \xi$. Blue dashed curve: model for the EoS of the unitary Fermi gas [above T_c: interpolation from the Monte Carlo calculation (*34*); below T_c: BCS theory, including phonon and pair-breaking excitations]. Green solid curve: effect of 2 μm optical resolution on the model EoS.

Department of Physics, Massachusetts Institute of Technology (MIT), MIT Harvard Center for Ultracold Atoms, and Research Laboratory of Electronics, MIT, Cambridge, MA 02139, USA.

*To whom correspondence should be addressed. E-mail: zwierlein@mit.edu

single-particle excitations freeze out and pairs form (see model in Fig. 1).

As $T \to 0$, the Fermi energy E_F is the only intensive energy scale, so the chemical potential must be related to E_F by a universal number, $\mu = \xi E_F$, where ξ is known as the Bertsch parameter (*6*, *7*). It follows that at $T = 0$, $\tilde{\kappa} = 1/\tilde{p} = 1/\xi$ (*13*). The extrapolation of the low-temperature experimental data for $\tilde{\kappa}(\tilde{p})$ toward the curve $\tilde{\kappa} = 1/\tilde{p}$ gives $\xi = 0.37(1)$, a value that we find consistently for the normalized chemical potential, energy, and free energy at our lowest temperatures.

From the universal function $\tilde{\kappa}(\tilde{p})$, we obtain all other thermodynamic quantities of the unitary gas. First, to find the normalized temperature T/T_F (where $k_B T_F = E_F$), note that the change in pressure with T/T_F at constant temperature is related to the compressibility. One finds $\frac{d\tilde{p}}{d(T/T_F)} = \frac{5}{2}\frac{T_F}{T}\left(\tilde{p} - \frac{1}{\tilde{\kappa}}\right)$, so by integration (*13*)

$$\frac{T}{T_F} = \left(\frac{T}{T_F}\right)_i exp\left\{\frac{2}{5}\int_{\tilde{p}_i}^{\tilde{p}} \mathrm{d}\tilde{p}\,\frac{1}{\tilde{p} - \frac{1}{\tilde{\kappa}}}\right\} \qquad (1)$$

where $(T/T_F)_i$ is the normalized temperature at an initial normalized pressure $\tilde{p}_i$ that can be chosen to lie in the Virial regime validated above.

Thanks to the relation $E = \frac{3}{2}P\mathcal{V}$, valid at unitarity (*17*), we can also directly obtain the heat capacity per particle at constant volume $\mathcal{V}$ (*13*),

$$\frac{C_V}{k_B N} \equiv \frac{1}{k_B N}\frac{\partial E}{\partial T}\Big|_{N,\mathcal{V}} = \frac{3}{5}\frac{\mathrm{d}\tilde{p}}{\mathrm{d}(T/T_F)} = \frac{3}{2}\frac{T_F}{T}\left(\tilde{p} - \frac{1}{\tilde{\kappa}}\right) \qquad (2)$$

Figure 2 shows the normalized compressibility and the specific heat as a function of T/T_F. At high temperatures, the specific heat approaches that of a noninteracting Fermi gas and eventually $C_V = \frac{3}{2} N k_B$, the value for a Boltzmann gas. A dramatic rise is observed for T/T_F at around 0.16, followed by a steep drop at lower temperatures. Such a λ-shaped feature in the specific heat is characteristic of second-order phase transitions, as in the famous λ transition in ^{4}He (*3*). Jumps in the specific heat are well known from superconductors (*1*) and ^{3}He (*2*). In experiments on atomic gases, such jumps had only been inferred from derivatives to fit functions that implied a jump (*20*, *21*). We do not expect to resolve the critical behavior very close to T_c. Because of the spatially varying chemical potential in our trapped sample, the critical region is confined to a narrow shell. Based on the estimate in (*22*), the thickness of the critical shell is 1% of the cloud size. The finite resolution of our imaging system (2 μm or about 5% of the cloud size in the radial direction) suffices to explain the rounding of the singularity expected from criticality. The rounding also reduces the observed jump in the heat capacity at the transition. We obtain a lower bound $\Delta C/C_n \equiv (C_s - C_n)/C_n \geq 1.0^{+4}_{-1}$, where C_s/N (C_n/N) is the specific heat per particle at the peak (the onset of the sudden rise). Considering the strong interactions, this is surprisingly close to the BCS value of 1.43 (*1*). Below T_c, the specific heat is expected to decrease as ~ $\exp(-\Delta_0/k_B T)$ due to the pairing gap Δ_0. At low temperatures, $T << T_c$, the phonon contribution $\propto T^3$ dominates (*23*). This behavior is consistent with our data, but the phonon regime is not resolved.

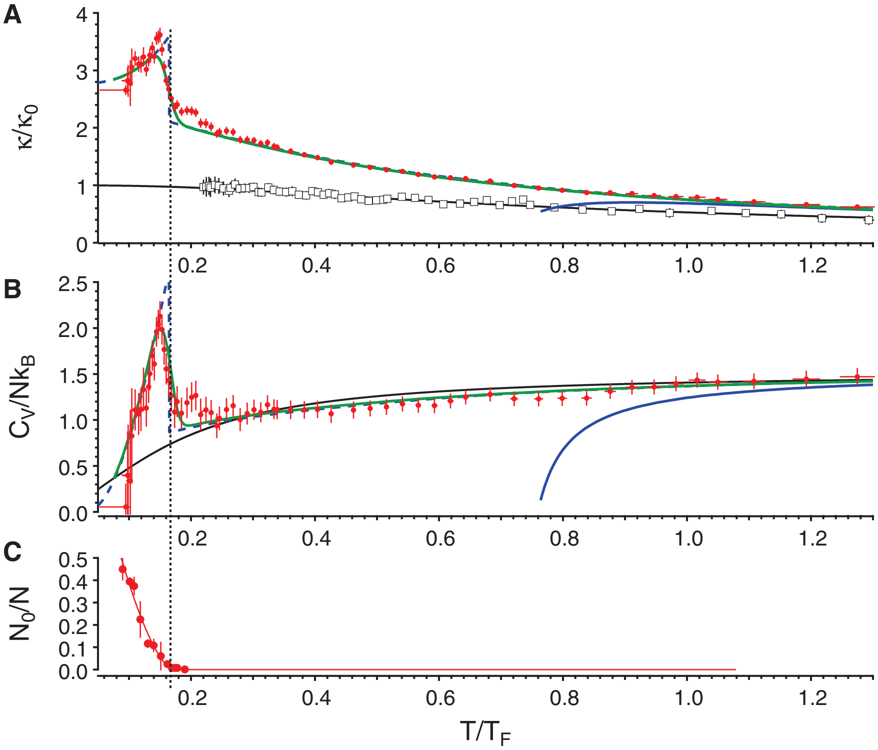

Fig. 2. (**A**) Normalized compressibility $\tilde{\kappa} = [2/3]\kappa\, n\, E_F$ and (**B**) specific heat per particle C_V/Nk_B of a unitary Fermi gas as a function of reduced temperature T/T_F (solid red circles). Black solid curve: theory for a noninteracting Fermi gas. Blue solid curve: third-order Virial expansion for the unitary gas. Black open squares: data for the normalized compressibility as a function of T/T_F of a noninteracting Fermi gas (combining data from both highly imbalanced gases at unitarity and balanced gases near zero-crossing). Blue dashed (green solid) curve: model from Fig. 1, excluding (including) the effect of finite imaging resolution. (**C**) Global condensate fraction at unitarity as determined from a rapid ramp to the molecular side of the Feshbach resonance, plotted as a function of local T/T_F at the trap center. The onset of condensation coincides with the sudden rise of the specific heat. Error bars, mean ± SD.

To validate our in situ measurements of the superfluid phase transition, we have employed the rapid ramp method to detect fermion pair condensation (*24*, *25*). The results (Fig. 2C) show that the onset of condensation and the sudden rise in specific heat and compressibility all occur at the same critical temperature, within the error bars. Unlike previous experimental determinations of T_c/T_F for the homogeneous unitary Fermi gas (*11*, *12*), we determine T_c/T_F directly from the density profiles, finding a sudden rise in the specific heat and the onset of condensation at $T_c/T_F = 0.167(13)$. This value is determined as the midpoint of the sudden rise, and the error is assessed as the shift due to the uncertainty of the Feshbach resonance (*13*). This is in very good agreement with theoretical determinations, such as the self-consistent T-matrix approach that gives $T_c/T_F \approx 0.16$ (*23*), and Monte Carlo calculations that give $T_c/T_F = 0.171(5)$ (*26*) and 0.152(7) (*27*). There is a current debate on the possibility of a pseudogap phase of preformed pairs above T_c (*12*, *28*). A pairing gap for single-particle excitations above the transition should be signaled by a downturn of the specific heat above T_c, which is not observed in our measurements.

From the definition of the compressibility $\kappa = \frac{1}{n^2}\frac{\partial n}{\partial \mu}\big|_T$, we can obtain the reduced chemical potential μ/E_F as a function of the T/T_F (Fig. 3A) (*13*). This function is here obtained from measured quantities, rather than from numerical derivatives of data that involved uncontrolled thermometry (*11*). In the interval of T/T_F from around 0.25 to 1, the chemical potential is close to that of a noninteracting Fermi gas, shifted by $(\xi_n - 1)E_F$ because of interactions present in the normal state, with $\xi_n \approx 0.45$. Unlike a normal Fermi gas, the chemical potential attains a maximum of $\mu/E_F = 0.42(1)$ at $T/T_F = 0.171(10)$, and then decreases at lower temperatures, as expected for a superfluid of paired fermions (*23*). As the temperature is increased from zero in a superfluid, first the emergence of phonons (sound excitations) and then the breaking of fermion pairs contribute to increasing the chemical potential. At T_c, the singular compressibility implies a sharp change in slope for μ/E_F, in agreement with our observation and theory (*23*). At low temperatures, the reduced chemical potential μ/E_F saturates to the universal value ξ. As the internal energy E and the free energy F satisfy $E(T) > E(0) = \frac{3}{5}N\xi E_F = F(0) > F(T)$ for all T, the reduced quantities $f_E \equiv \frac{5}{3}\frac{E}{NE_F} = \tilde{p}$ and $f_F \equiv \frac{5}{3}\frac{F}{NE_F} = \frac{5}{3}\frac{\mu}{E_F} - \frac{2}{3}\tilde{p}$ (Fig. 3A) provide upper and lower bounds for ξ (*29*). Taking the coldest points of these three curves and including the systematic error due to the effective interaction range, we find $\xi = 0.376(4)$. The uncertainty in the Feshbach resonance is expected to shift ξ by at most 2% (*13*). This value is consistent with a recent upper bound $\xi < 0.383(1)$ from (*30*), is close to $\xi = 0.36(1)$ from a self-consistent T-matrix calculation (*23*), and agrees with $\xi = 0.367(9)$ from an epsilon expansion (*31*). It lies below earlier estimates $\xi = 0.44(2)$ (*32*) and $\xi = 0.42(1)$ (*33*) from fixed-node quantum Monte Carlo calculation that provides upper bounds on ξ. Our measurement agrees with several less accurate experimental determinations (*6*) but disagrees with the most recent experimental value 0.415(10) that was used to calibrate the pressure in (*12*).

From the energy, pressure, and chemical potential, we can obtain the entropy $S = \frac{1}{T}(E + PV - \mu N)$, and hence the entropy per particle $S/Nk_B =$

$$\frac{T_F}{T}\left(\tilde{p} - \frac{\mu}{E_F}\right)$$ as a function of T/T_F (Fig. 3B). At high temperatures, S is close to the entropy of an ideal Fermi gas at the same T/T_F. Above T_c, the entropy per particle is nowhere small compared with k_B. Also, the specific heat C_V is not linear in T in the normal phase. This shows that the normal regime above T_c cannot be described in terms of a Landau Fermi Liquid picture, although some thermodynamic quantities agree surprisingly well with the expectation for a Fermi liquid [see (*12*) and (*13*)]. Below about $T/T_F = 0.17$, the entropy starts to strongly fall off compared with that of a noninteracting Fermi gas, which we again interpret as the freezing out of single-particle excitations as a result of the formation of fermion pairs. Far below T_c, phonons dominate. They only have a minute contribution to the entropy (*23*), less than 0.02 k_B at $T/T_F = 0.1$, consistent with our measurements. At the critical point, we obtain $S_c = 0.73(13)$ Nk_B, in agreement with theory (*23*). It is encouraging for future experiments with fermions in optical lattices that we obtain entropies less than 0.04 N k_B, far below critical entropies required to reach magnetically ordered phases.

From the chemical potential μ/E_F and $T/T_F = \frac{4\pi}{(3\pi^2)^{2/3}}\frac{1}{(n\lambda^3)^{2/3}}$, we finally obtain the density EoS $n(\mu,T) \equiv \frac{1}{\lambda^3}f_n(\beta\mu)$, with the de Broglie wavelength $\lambda = \sqrt{\frac{2\pi\hbar^2}{mk_BT}}$. The pressure EoS follows as $P(\mu,T) \equiv \frac{k_BT}{\lambda^3}f_P(\beta\mu)$, with $f_P = \frac{2}{5}\frac{T_F}{T}\tilde{p}f_n(\beta\mu)$. Figure 4 shows the density and pressure normalized by their noninteracting counterparts at the same chemical potential and temperature. For the normal state, a concurrent theoretical calculation employing a new Monte Carlo method agrees excellently with our data (*34*). Our data deviate from a previous experimental determination of the pressure EoS (*12*) that was calibrated with an independently measured value of $\xi = 0.415(10)$ (*35*) and disagree with the energy measurement in (*11*) that used a thermometry inconsistent with the Virial expansion (*10*). Around

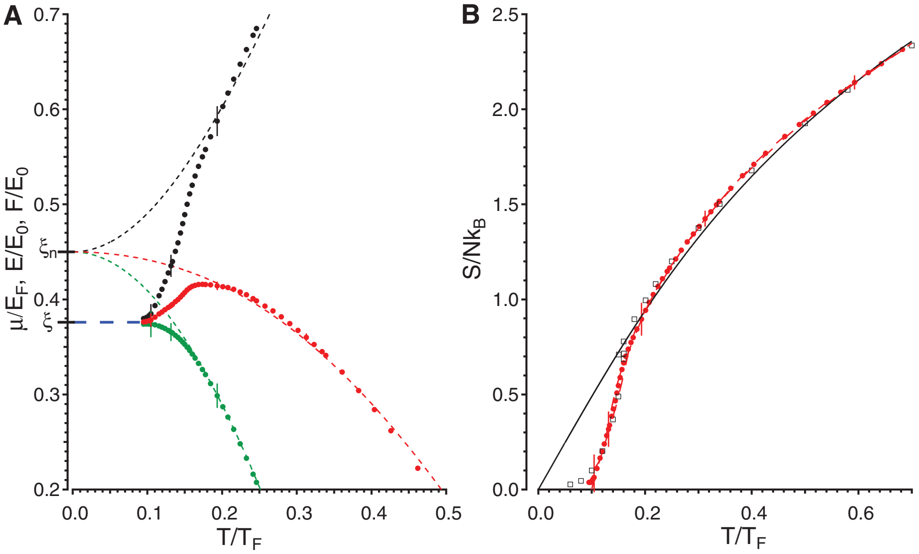

Fig. 3. (**A**) Chemical potential μ, energy E, and free energy F of the unitary Fermi gas versus T/T_F. μ (red solid circles) is normalized by the Fermi energy E_F, and E (black solid circle) and F (green solid circle) are normalized by $E_0 = \frac{3}{5}N\ E_F$. At high temperatures, all quantities approximately track those for a noninteracting Fermi gas, shifted by $\xi_n - 1$ (dashed curves). The peak in the chemical potential signals the onset of superfluidity. In the deeply superfluid regime at low temperatures, μ/E_F, E/E_0, and F/F_0 all approach ξ (blue dashed line). (**B**) Entropy per particle. At high temperatures, the entropy closely tracks that of a noninteracting Fermi gas (black solid curve). The open squares are from the self-consistent T-matrix calculation (*23*). A few representative error bars are shown, representing mean ± SD.

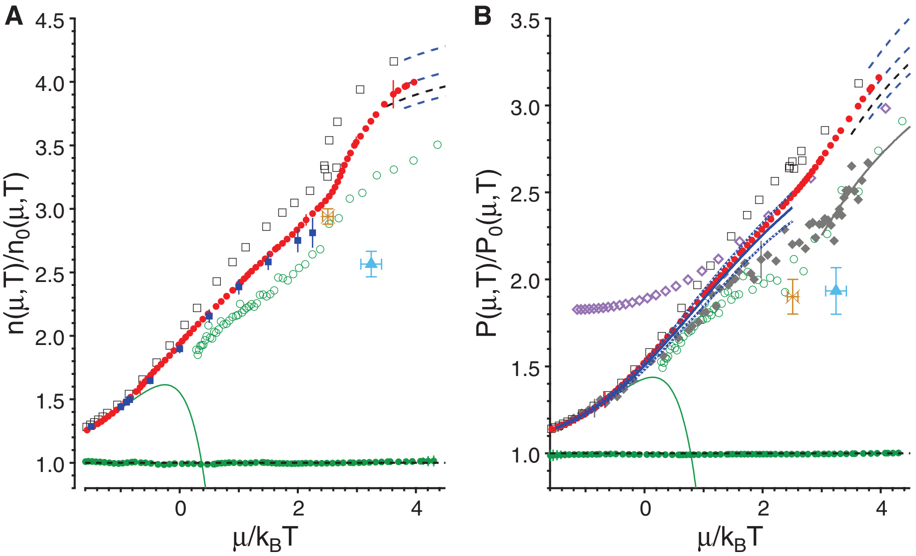

Fig. 4. (**A**) Density and (**B**) pressure of a unitary Fermi gas versus $\mu/k_B T$, normalized by the density and pressure of a noninteracting Fermi gas at the same chemical potential μ and temperature T. Red solid circles: experimental EoS. Blue dashed curves: low-temperature behavior with $\xi = 0.364$ (upper), 0.376 (middle), and 0.388 (lower). Black dashed curve: low-temperature behavior with ξ at upper bound of 0.383 from (*30*). Green solid circles (black fine dashed line): MIT experimental data (theory) for the ideal Fermi gas. Blue solid squares (blue curve): diagrammatic Monte Carlo calculation (*34*) for density (pressure, with blue dashed curves denoting the uncertainty bands). Solid green line: third-order Virial expansion. Open black squares: self-consistent T-matrix calculation (*23*). Open green circles: lattice calculation (*36*). Orange star and blue triangle: critical point from the Monte Carlo calculations (*26*) and (*27*), respectively. Solid diamonds: Ecole Normale Supérieure experiment (*12*). Purple open diamonds: Tokyo experiment (*11*).

the critical point, the density shows a strong variation, whereas the pressure, the integral of the density over μ at constant *T*, is naturally less sensitive to the superfluid transition.

In conclusion, we have performed thermodynamic measurements of the unitary Fermi gas across the superfluid phase transition at the level of uncertainty of a few percent, without any fits or input from theory, enabling validation of theories for strongly interacting matter. Similar unbiased methods can be applied to other systems, for example, two-dimensional Bose and Fermi gases or fermions in optical lattices.

References and Notes

1. M. Tinkham, *Introduction to Superconductivity* (Dover, Mineola, New York, ed. 2, 2004).
2. D. Vollhardt, P. Wölfle, *The Superfluid Phases of Helium 3* (Taylor & Francis, London, 1990).
3. J. A. Lipa, J. A. Nissen, D. A. Stricker, D. R. Swanson, T. C. P. Chui, *Phys. Rev. B* **68**, 174518 (2003).
4. M. W. Zwierlein, J. R. Abo-Shaeer, A. Schirotzek, C. H. Schunck, W. Ketterle, *Nature* **435**, 1047 (2005).
5. W. Ketterle, M. Zwierlein, *Riv. Nuovo Cim.* **31**, 247 (2008).
6. S. Giorgini, L. P. Pitaevskii, S. Stringari, *Rev. Mod. Phys.* **80**, 1215 (2008).
7. I. Bloch, J. Dalibard, W. Zwerger, *Rev. Mod. Phys.* **80**, 885 (2008).
8. J. Kinast *et al.*, *Science* **307**, 1296 (2005).
9. J. T. Stewart, J. P. Gaebler, C. A. Regal, D. S. Jin, *Phys. Rev. Lett.* **97**, 220406 (2006).
10. L. Luo, B. Clancy, J. Joseph, J. Kinast, J. E. Thomas, *Phys. Rev. Lett.* **98**, 080402 (2007).
11. M. Horikoshi, S. Nakajima, M. Ueda, T. Mukaiyama, *Science* **327**, 442 (2010).
12. S. Nascimbène, N. Navon, K. J. Jiang, F. Chevy, C. Salomon, *Nature* **463**, 1057 (2010).
13. Materials and methods are available as supporting material on *Science* Online.
14. Y. Shin, M. W. Zwierlein, C. H. Schunck, A. Schirotzek, W. Ketterle, *Phys. Rev. Lett.* **97**, 030401 (2006).
15. G. B. Partridge *et al.*, *Phys. Rev. Lett.* **97**, 190407 (2006).
16. C.-H. Cheng, S.-K. Yip, *Phys. Rev. B* **75**, 014526 (2007).
17. T.-L. Ho, *Phys. Rev. Lett.* **92**, 090402 (2004).
18. X.-J. Liu, H. Hu, P. D. Drummond, *Phys. Rev. Lett.* **102**, 160401 (2009).
19. D. Rakshit, K. M. Daily, D. Blume, Thermodynamics of two-component Fermi gas with large scattering length: Fourth- and higher-order virial coefficients, preprint arXiv:1106.5958; available at http://arxiv.org/abs/1106.5958.
20. J. R. Ensher, D. S. Jin, M. R. Matthews, C. E. Wieman, E. A. Cornell, *Phys. Rev. Lett.* **77**, 4984 (1996).
21. L. Luo, J. Thomas, *J. Low Temp. Phys.* **154**, 1 (2009).
22. L. Pollet, N. V. Prokof'ev, B. V. Svistunov, *Phys. Rev. Lett.* **104**, 245705 (2010).
23. R. Haussmann, W. Rantner, S. Cerrito, W. Zwerger, *Phys. Rev. A* **75**, 023610 (2007).
24. C. A. Regal, M. Greiner, D. S. Jin, *Phys. Rev. Lett.* **92**, 040403 (2004).
25. M. W. Zwierlein *et al.*, *Phys. Rev. Lett.* **92**, 120403 (2004).
26. O. Goulko, M. Wingate, *Phys. Rev. A* **82**, 053621 (2010).
27. E. Burovski, N. Prokof'ev, B. Svistunov, M. Troyer, *Phys. Rev. Lett.* **96**, 160402 (2006).
28. J. P. Gaebler *et al.*, *Nat. Phys.* **6**, 569 (2010).
29. Y. Castin, F. Werner, *The BCS-BEC Crossover and the Unitary Fermi Gas*, W. Zwerger, ed. (Springer-Verlag, Berlin, 2012), chap. 5.
30. M. M. Forbes, S. Gandolfi, A. Gezerlis, *Phys. Rev. Lett.* **106**, 235303 (2011).
31. P. Arnold, J. E. Drut, D. T. Son, *Phys. Rev. A* **75**, 043605 (2007).
32. J. Carlson, S.-Y. Chang, V. R. Pandharipande, K. E. Schmidt, *Phys. Rev. Lett.* **91**, 050401 (2003).
33. G. E. Astrakharchik, J. Boronat, J. Casulleras, A. S. Giorgini, *Phys. Rev. Lett.* **93**, 200404 (2004).
34. K. Van Houcke *et al.*, Feynman diagrams versus Fermi-gas Feynman quantum emulator, preprint arXiv:1110.3747 (2011); available at http://arxiv.org/abs/1110.3747.
35. S. Nascimbène, Thermodynamics of ultracold Fermi gases, thesis, Ecole Normale Supérieure, Paris (2010).
36. A. Bulgac, J. E. Drut, P. Magierski, *Phys. Rev. Lett.* **96**, 090404 (2006).

Acknowledgments: We thank B. Svistunov, N. Prokof'ev, and F. Werner for fruitful discussions; Z. Hadzibabic for a critical reading of the manuscript; the authors of (*11*, *12*, *23*, *26*, *27*, *36*) for kindly providing us with their data; and André Schirotzek for help during the early stages of the experiment. M.J.H.K. acknowledges financial support from NSERC. This work was supported by the NSF, Air Force Office of Scientific Research (AFOSR) - Multidisciplinary Research Program of the University Research Initiative (MURI), Army Research Office (ARO) - MURI, Office of Naval Research, Defense Advanced Research Projects Agency (DARPA) Young Faculty Award, a grant from the ARO with funding from the DARPA Optical Lattice Emulator program, an AFOSR Presidential Early Career Award in Science and Engineering, the David and Lucile Packard Foundation, and the Alfred P. Sloan Foundation.

Supporting Online Material
www.sciencemag.org/cgi/content/full/science.1214987/DC1
Materials and Methods
Figs. S1 to S4
References (*37–45*)

7 October 2011; accepted 3 January 2012
Published online 12 January 2012;
10.1126/science.1214987

Iron Catalysts for Selective Anti-Markovnikov Alkene Hydrosilylation Using Tertiary Silanes

Aaron M. Tondreau,[1] Crisita Carmen Hojilla Atienza,[1] Keith J. Weller,[2] Susan A. Nye,[2] Kenrick M. Lewis,[3] Johannes G. P. Delis,[4] Paul J. Chirik[1]*

Alkene hydrosilylation, the addition of a silicon hydride (Si-H) across a carbon-carbon double bond, is one of the largest-scale industrial applications of homogeneous catalysis and is used in the commercial production of numerous consumer goods. For decades, precious metals, principally compounds of platinum and rhodium, have been used as catalysts for this reaction class. Despite their widespread application, limitations such as high and volatile catalyst costs and competing side reactions have persisted. Here, we report that well-characterized molecular iron coordination compounds promote the selective anti-Markovnikov addition of sterically hindered, tertiary silanes to alkenes under mild conditions. These Earth-abundant base-metal catalysts, coordinated by optimized bis(imino)pyridine ligands, show promise for industrial application.

Metal-catalyzed olefin hydrosilylation, which forms alkylsilanes by cleaving a silicon-hydrogen bond and adding the fragments across a carbon-carbon double bond (*1*, *2*), finds widespread application in the commercial manufacture of silicone-based surfactants, fluids, molding products, release coatings, and pressure-sensitive adhesives (*3*, *4*). Consequently, hydrosilylation has emerged as one of the largest-scale applications of homogeneous catalysis (*5*–*9*). For more than three decades, precious metal compounds with Pt, Pd, Ru, and Rh have been used almost exclusively as catalysts. Platinum compounds such as Karstedt's and Speier's catalysts, $Pt_2\{[(CH_2{=}CH)SiMe_2]_2O\}_3$ (Me, methyl) and $H_2PtCl_6{\cdot}6H_2O/{}^iPrOH$ (^{i}Pr, isopropyl), respectively, are the most widely used industrial catalysts (*1*, *10*–*12*), though they suffer from chemical limitations such as intolerance to amino-substituted olefins and a tendency to catalyze competing isomerization of the terminal alkenes to internal isomers. Undesired isomerization often necessitates subsequent purification steps that are both energy and cost intensive. Furthermore, decomposition of the catalyst to colloidal platinum contributes to unwanted side reactions and also causes discoloration of the final products.

It has been estimated that the worldwide silicone industry consumed ~180,000 troy ounces (5.6 metric tons) of platinum in 2007 and most is not recovered (*13*). The high cost, coupled with the increasing demands on precious metals due to fuel-cell and other emerging technologies, has increased the volatility of the platinum market (*14*). The combination of chemical, economic, and political challenges inspires the exploration of inexpensive and Earth-abundant catalysts using iron, manganese, and cobalt (*15*). At the core of this challenge is suppressing tendencies of first-row transition metals toward one-electron redox processes in favor of the two-electron chemistry associated with the heavier metals that probably make up the fundamental steps in a catalytic cycle for alkene hydrosilylation.

---

[1] Department of Chemistry, Princeton University, Princeton, NJ 08544, USA. [2] Momentive Performance Materials, 260 Hudson River Road, Waterford, NY 12188, USA. [3] Momentive Performance Materials, 769 Old Saw Mill River Road, Tarrytown, NY 10591, USA. [4] Momentive Performance Materials bv, Plasticslaan 1, 4612PX Bergen op Zoom, Netherlands.

*To whom correspondence should be addressed. E-mail: pchirik@princeton.edu